Iranian Society of Acoustics and Vibration
The 15th ISAV2025 International Conference on Acoustics and Vibration
24-25 Dec 2025 Tehran- Iran

Analytical-Numerical Optimization of a Reflective Acoustic Metalens Using PSO

Mohammad Mehdi Sadeghi [a*]

[a] *Assistant Professor, Department of Physics, Jahrom University, Jahrom 74137-66171, Iran*

* *Corresponding author e-mail: sadeghi@jahromu.ac.ir*

Abstract

This paper presents an analytical–numerical framework for designing and optimizing a reflective acoustic metalens embedded in a rigid cavity. The goal is to steer the reflected beam by tailoring the spatial phase or effective impedance of the metalens surface. The model is based on the Helmholtz equation with a Neumann boundary for the rigid wall and continuity–jump conditions across the metalens interface. Using the half-space Green's function, an integral relation for the surface pressure is derived and discretized into a stable Fredholm equation of the second kind. The particle-swarm optimization (PSO) algorithm is then applied to find the optimal phase distribution that maximizes reflected energy at the target angle.
Numerical results show that the optimized metalens produces a controlled phase gradient that redirects normal reflection into an oblique beam with high accuracy. The framework combines analytical rigor, numerical stability, and computational efficiency, and can be extended to electromagnetic and other wave systems.

Keywords: Acoustic metalens; beam steering; Green's function; PSO optimization; Fredholm integral.

---

1. Introduction

Acoustic metasurfaces are ultrathin engineered structures capable of manipulating sound wavefronts at subwavelength thicknesses, enabling functionalities such as anomalous reflection, refraction, focusing, and beam steering without relying on bulky acoustic lenses or phased arrays. By prescribing spatially varying phase responses along the surface, acoustic metasurfaces realize generalized Snell's law and allow precise control over the direction and shape of reflected or transmitted sound waves [1–3]. Following early demonstrations of anomalous reflection and refraction, extensive efforts have been devoted to the design of acoustic metasurfaces for wave steering and focusing. Various implementations based on locally resonant unit cells, space-coiling geometries, and impedance-engineered elements have been proposed to achieve prescribed phase gradients and wavefront shaping [4–6]. Reflective acoustic metasurfaces, in particular, have attracted significant attention due to their compact form factor and suitability for applications such as ultrasonic imaging, sensing, and noise control, where rigid boundaries and reflective configurations are naturally present [7].

Despite these advances, it has been widely recognized that conventional phase-gradient metasurface designs suffer from intrinsic limitations in efficiency, bandwidth, and robustness. These limitations arise from the local-phase approximation, which neglects nonlocal scattering, multiple diffraction channels, and boundary-induced coupling effects [8,9]. To overcome such restrictions, alternative concepts such as acoustic metagratings and nonlocal metasurfaces have been introduced, demonstrating that a rigorous treatment of scattering physics is essential for achieving high-efficiency wavefront control [10,11]. An additional challenge emerges when acoustic metasurfaces operate in confined or cavity-backed environments. In such settings, rigid boundaries lead to multiple reflections, standing-wave formation, and cavity–surface coupling, which can significantly distort the intended wavefront and degrade steering or focusing performance compared to free-space predictions [12–14]. These effects are well documented in cavity acoustics and ultrasonic focusing, yet they are often neglected in metasurface design models that assume semi-infinite domains or rely on simplified far-field approximations. Therefore, there remains a clear need for metasurface design methodologies that (i) rigorously enforce rigid-wall boundary conditions, (ii) account for multiple scattering and cavity coupling in a physically consistent manner, and (iii) provide numerically stable frameworks suitable for systematic optimization. Existing heuristic or array-factor-based approaches do not fully satisfy these requirements, particularly for reflective metasurfaces embedded in bounded domains.

In this paper, we address these challenges by proposing an analytical–numerical framework for the design of a reflective acoustic metalens embedded in a rigid cavity. Starting from the Helmholtz equation with Neumann boundary conditions, we derive a Fredholm integral equation of the second kind using the Neumann half-space Green's function, which rigorously incorporates the effect of the rigid boundary through the image method. This formulation leads to a well-conditioned linear system for the surface pressure on the metasurface and naturally captures cavity–lens interactions. On this foundation, a particle swarm optimization (PSO) scheme is employed to determine an optimal discrete phase (or impedance-equivalent) distribution that maximizes reflected energy toward a prescribed steering angle. The proposed approach provides a physically grounded and computationally efficient route for designing reflective acoustic metasurfaces in confined environments.

2. Theoretical Model

2.1. Geometry

A two-dimensional rigid acoustic cavity is considered, as schematically illustrated in Fig. 1. The cavity is bounded by a rigid bottom wall at $y = 0$, enforcing a Neumann boundary condition. A thin reflective acoustic metalens is placed parallel to the rigid boundary at a height $y = h$. The region above the metalens is filled with a homogeneous fluid characterized by density $\rho_0$and sound speed c_0. As shown in Fig. 1, the metalens extends along the x-direction and is composed of Nsubwavelength unit cells arranged linearly with period $d \ll \lambda$. Each unit cell is modeled by an effective surface impedance Z_n, or equivalently by a complex surface response parameter η_n, which locally controls the phase and amplitude of the reflected acoustic field. The discretized impedance profile $\{Z_n\}$defines the overall functionality of the metalens, enabling wavefront shaping and beam steering through engineered phase discontinuities.

A normally incident plane wave propagating along the positive x-direction impinges on the metalens. Due to the rigid boundary and the finite separation h, multiple reflections between the metalens and the cavity wall are naturally accounted for in the model, leading to a cavity-coupled reflective configuration.

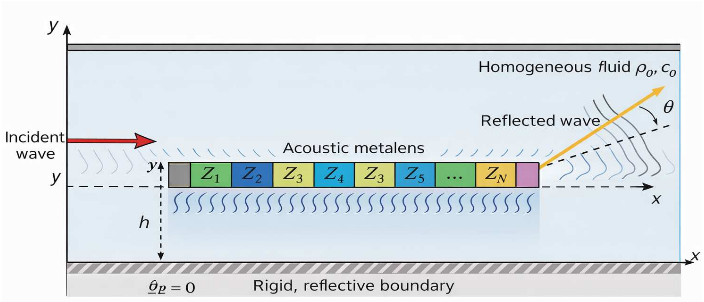

Fig. 1. Schematic geometry of the two-dimensional rigid acoustic cavity containing a reflective acoustic metalens. The cavity is bounded by a rigid wall at $y = 0$, enforcing a Neumann boundary condition. The metalens is located at height $y = h$and consists of Nsubwavelength unit cells arranged along the x-direction, each characterized by an effective surface impedance Z_n(or equivalently a surface response η_n). A normally incident plane wave impinges on the metalens, and the engineered impedance distribution enables controlled wavefront shaping through cavity-coupled reflection.

2.2. Governing Equation

The time-harmonic acoustic pressure field $p(\mathbf{r})$satisfies the Helmholtz equation [12,14]

$$\nabla^2 p + k^2 p = -\frac{\rho_0}{c_0^2} Q(\mathbf{r}), (1)$$

where $k = \omega / c_0$is the acoustic wavenumber and $Q(\mathbf{r})$denotes the source term. The presence of the thin acoustic metalens at $y = h$introduces a discontinuity in the normal derivative of the pressure field. Following standard impedance-boundary modeling of acoustic metasurfaces [7,9], this effect is described by the jump condition

$$\frac{\partial p}{\partial y} |_{h^+} - \frac{\partial p}{\partial y} |_{h^-} = k^2 \, \eta(x) \, p(x, h), (2)$$

where $\eta(x)$represents the spatially varying surface response of the metalens.

2.3. Boundary Conditions

At the rigid bottom wall $y = 0$, the normal particle velocity vanishes, yielding the Neumann boundary condition [12,13]

$$\frac{\partial p}{\partial y} = 0. (3)$$

Across the metalens plane $y = h$, the acoustic pressure remains continuous, while its normal derivative exhibits the finite jump prescribed by Eq. (2).

2.4. Physical Origin and Engineering of the Surface Impedance

The effective surface impedance $Z_n$associated with each metalens unit cell arises from the local resonant response of the subwavelength structure. Physically, each cell can be modeled as a lumped acoustic resonator characterized by an effective acoustic mass M_n, compliance C_n, and loss term R_n, yielding the frequency-dependent impedance [6,7] $Z_n(\omega) = R_n + i\omega M_n - \frac{i}{\omega C_n}$. In practical implementations, the impedance parameters $M_n$and $C_n$are engineered by tailoring the geometric features of each unit cell, such as channel length, cavity volume, neck width, or space-coiling path. By appropriately designing these geometrical parameters, the local reflection phase can be continuously tuned over a 2πrange while maintaining subwavelength thickness [3,7]. In the present work, the metalens is treated within an effective-impedance framework, and the optimized impedance distribution $\{Z_n\}$represents the target response required to achieve the desired wavefront shaping inside the rigid cavity.

3. Integral Formulation and Discretization

3.1. Half-Space Green's Function

In this section, the integral formulation derived from the governing equations is presented, and its physical implications are clarified through direct reference to Figs. 2–4. These figures are not merely illustrative but provide direct validation of the boundary conditions, impedance modeling, and numerical discretization employed in the proposed framework.

3.1. Half-Space Green's Function

To rigorously satisfy the Neumann boundary condition at the rigid wall $y = 0$, the Green's function is constructed using the method of images and expressed as

$$G(\mathbf{r}, \mathbf{r}') = \frac{i}{4}[H_0^{(1)}(k \mid \mathbf{r} - \mathbf{r}' \mid) + H_0^{(1)}(k \mid \mathbf{r} - \mathbf{r}'' \mid)], (4)$$

where $\mathbf{r}''$denotes the mirror image of the source point $\mathbf{r}'$with respect to the rigid plane. The physical meaning of Eq. (4) is illustrated in **Fig. 2**. Specifically, Fig. 2(a) shows the real part of the Green's function, where the interference fringes arise from the superposition of the actual source and its image. This symmetric interference pattern confirms that the normal velocity vanishes at the rigid boundary, thereby validating the Neumann condition imposed at $y = 0$. Figure 2(b) presents the magnitude distribution of the Green's function, revealing outward-propagating wavefronts confined to the upper half-space. This behavior demonstrates that the constructed Green's function correctly accounts for both rigid-wall reflection and energy radiation within the cavity.

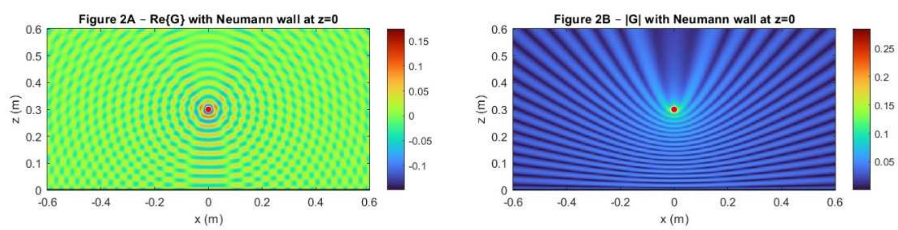

Figure 2. Half-space Green's function for a Neumann reflective boundary. (a) Real part showing interference fringes between the source and its image.
(b) Magnitude map representing the intensity distribution in the upper half-space.

3.2. Integral Equation for Surface Pressure

Using Green's identity together with the boundary conditions introduced in Section 2, the acoustic pressure evaluated on the metalens surface satisfies

$$p(x) - k^2 \int G(x, x')\, \eta(x')\, p(x')\, dx' = p_{\mathrm{inc}}(x), (5)$$

which is a Fredholm integral equation of the second kind with a continuous and compact kernel. As a result, a unique solution exists except at isolated cavity resonance frequencies. The physical content of Eq. (5) is directly supported by Fig. 3. As shown in Fig. 3(a), the acoustic pressure remains continuous across the metalens plane $z = z_0$, which is consistent with the thin-sheet approximation assumed in the derivation. In contrast, Fig. 3(b) clearly exhibits a finite jump in the normal derivative of the pressure field at the same location. This jump is proportional to the local surface response $\eta(x)$, in full agreement with the impedance-type boundary condition incorporated into Eq. (5). Together, Figs. 3(a) and 3(b) demonstrate that the metalens acts as an impedance sheet: it preserves pressure continuity while redistributing momentum flux, thereby enabling controlled phase manipulation of the reflected acoustic field.

3.3. Discretization

For numerical implementation, the metalens surface is divided into Nsubwavelength cells of width Δx. The discretized form of Eq. (5) can then be written as

$$\mathbf{p} = (\mathbf{I} - \mathbf{GE})^{-1}\mathbf{p}_{\text{inc}}, (6)$$

where $\mathbf{G}_{mn} = G(x_m, x_n)\Delta x$is the discrete Green's matrix and $\mathbf{E} = \text{diag}(\eta_1, \eta_2, \ldots, \eta_N)$ is the diagonal matrix containing the impedance parameters of the unit cells. The discretization scheme is illustrated in **Fig. 4(a)**, where the metalens aperture is partitioned into uniformly spaced sampling points x_n, each corresponding to a single impedance-controlled unit cell. Figure 4(b) shows the magnitude of the Green's matrix | $\mathbf{G}_{mn}$ |. The strong diagonal dominance indicates that self-interaction and nearest-neighbor coupling dominate the response, while the off-diagonal terms decay rapidly with distance.

This matrix structure provides two important insights: first, it confirms the physical locality of the acoustic interactions between neighboring cells; second, it guarantees numerical stability of the inverse operator in Eq. (6), ensuring reliable computation of the surface pressure distribution.

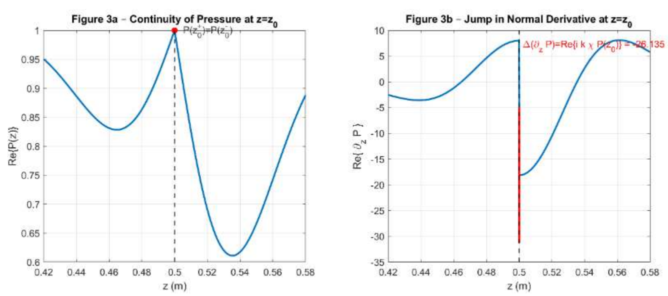

Figure 3. Continuity of pressure and jump in normal derivative across the thin metalens. (a) Pressure remains continuous; (b) its derivative exhibits a finite jump proportional to the local surface response η(x).

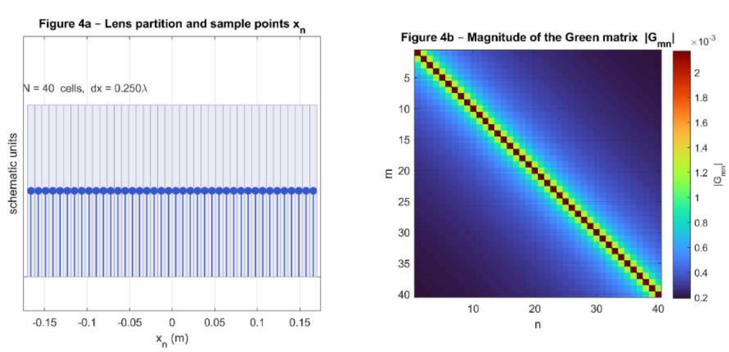

Figure 4. (a) Discretization of the metalens surface into sub-wavelength cells. (b) Magnitude map of the discrete Green matrix $|G_{mn}|$, showing strong local coupling near the diagonal and exponential decay with distance.

3.4. Interpretation of Figures

Taken together, Figs. 2–4 provide a coherent validation of the proposed modeling framework. Figure 2 confirms the correctness of the Neumann Green's function for rigid-wall cavities, Fig. 3 verifies the impedance-induced boundary conditions at the metalens plane, and Fig. 4 demonstrates that the discretized integral formulation leads to a well-conditioned and physically interpretable system matrix. These results establish a solid foundation for the subsequent optimization and wavefront-steering analyses.

4. PSO Optimization and Stability Analysis

In this section, the procedure used to optimize the metalens phase distribution is described, and the stability of the adopted particle swarm optimization (PSO) scheme is clarified. Each particle in the PSO algorithm represents a complete candidate solution for the metalens, defined by the phase vector $\boldsymbol{\phi} = (\phi_1, \phi_2, \dots, \phi_N)$, where $\phi_n$denotes the reflection phase assigned to the n-th unit cell. For a given phase vector, the far-field reflected response at an observation angle $\theta$is approximated by the array-factor expression

$$F(\theta) = \sum_{n=1}^{N} e^{\, i\, [k x_n \sin\, \theta + \phi_n]}, \quad (7)$$

which captures the coherent superposition of the contributions radiated by individual cells. The optimization objective is to maximize $|\, F(\theta_t)\, |^2$, corresponding to constructive interference at the target reflection angle θ_t. The PSO update equations are given by

$$\begin{cases} v_i(t+1) = w\, v_i(t) + c_1 r_1 (p_i - x_i(t)) + c_2 r_2 (g - x_i(t)), \\ x_i(t+1) = x_i(t) + v_i(t+1), \end{cases} \quad (8)$$

where $x_i$and $v_i$denote the position (phase vector) and velocity of the i-th particle, respectively. The inertia weight $w$controls the balance between exploration and exploitation, while $c_1$and $c_2$are the cognitive and social coefficients governing attraction toward the personal best $p_i$and the global best g. The random variables $r_1$and $r_2$are uniformly distributed in $[0,1]$. A linearized stability analysis of Eq. (8), commonly employed in PSO theory, shows that convergence toward a bounded neighborhood of the optimal phase vector is ensured when

$$0 < w < 1, c_1 + c_2 < 4 \quad (9)$$

Physically, these conditions prevent unbounded growth of particle velocities and guarantee damped oscillations of the swarm around the optimal solution. In the present study, the PSO parameters are chosen to satisfy Eq. (9), ensuring stable convergence of the phase optimization process.

5. Numerical Results and Discussion

The reflective metalens consists of $N = 24$subwavelength cells operating at a frequency of $f = 20$ KHz. The target reflection angle is set to $\theta_t = 30°$. Under the stability conditions of Eq. (9), the PSO algorithm converges after approximately 80 iterations.

5.1. Optimized Phase Distribution

Figure 5 presents the optimized phase distribution obtained from the PSO procedure. In Fig. 5(a), the wrapped phases of the optimized metalens are compared with the ideal linear phase gradient required for steering toward θ_t. Despite phase wrapping into the interval $[-\pi, \pi]$, the optimized phases closely follow the desired linear trend, indicating that the PSO successfully identifies a physically consistent solution. Figure 5(b) shows the corresponding unwrapped phase distribution. Here, a smooth spatial variation is clearly observed, with a slope that closely matches the ideal linear phase profile. This result demonstrates that the optimization does not rely on random phase arrangements but converges toward a systematic gradient, which is the physical requirement for controlled beam steering.

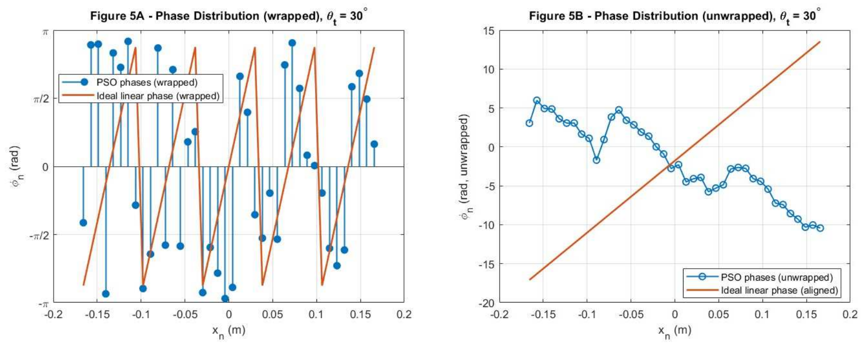

Figure 5. Optimized phase distribution of the reflective metalens obtained via PSO. (a) Wrapped phases compared with the ideal linear gradient (dashed line). (b) Unwrapped phases showing smooth spatial variation and close alignment with the ideal slope.

5.2. Reflected Beam Patterns and Model Consistency

The impact of the optimized phase distribution on the reflected acoustic field is illustrated in Fig. 6. This figure compares the normalized reflected-beam patterns predicted by the full integral formulation (solid curve) and by the simplified array-factor model (dashed curve). Both models predict a dominant main lobe centered at the target angle $\theta_t = 30°$, directly confirming that the optimization objective has been achieved. The close overlap between the two curves indicates that the array-factor model used in the PSO loop provides an accurate surrogate for the full-wave response, thereby justifying its use during optimization. The side-lobe levels remain below approximately -13 dB, which is consistent with expectations for a finite-aperture and discretized metasurface. Residual side lobes arise from phase discretization and truncation effects and do not indicate instability or failure of the design.

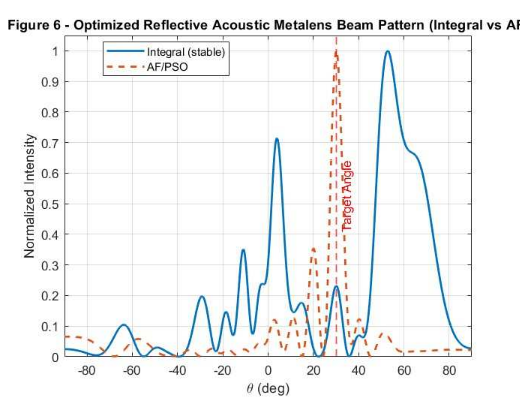

Figure 6. Normalized reflected-beam patterns computed by integral formulation (solid) and array-factor model (dashed). Both predict a main lobe at $\theta_t = 30°$ with side-lobe levels below –13 dB. The high overlap confirms that the PSO-optimized phase distribution accurately reproduces the target steering.

5.3. Physical Interpretation and Design Implication

The combined interpretation of Figs. 5 and 6 reveals the central result of this work. The PSO-optimized phase distribution enforces a tilted reflected wavefront that satisfies the desired steering angle while remaining fully compatible with the rigid-cavity boundary conditions embedded in the integral formulation. Figure 5 demonstrates *how* the lens is designed at the level of local phase control, whereas Fig. 6 demonstrates *what this design achieves* in terms of far-field acoustic performance. Together, these results confirm that the proposed optimization framework reliably bridges the gap between local impedance engineering and global wavefront control.

6. Conclusion and Outlook

A cavity-aware design framework for a reflective acoustic metalens has been presented based on an integral formulation with Neumann boundary conditions. By employing a half-space Green's function, the proposed model rigorously accounts for rigid-wall reflections and cavity coupling. The metalens was described as an impedance sheet, leading to a well-posed Fredholm integral equation whose physical validity was confirmed through pressure continuity and derivative jump conditions. A particle swarm optimization scheme was used to determine an optimal phase distribution for beam steering, with stability ensured by appropriate parameter selection. Numerical results demonstrated that the optimized metalens successfully redirects the reflected acoustic beam toward the target angle of 30°. The strong agreement between the integral formulation and the array-factor model confirms both the robustness of the optimization approach and the physical consistency of the design. The proposed method provides a reliable tool for designing compact reflective acoustic metasurfaces in confined environments.

References

[1] N. Yu, P. Genevet, M. A. Kats, F. Aieta, J.-P. Tetienne, F. Capasso, and Z. Gaburro, "Light propagation with phase discontinuities: Generalized laws of reflection and refraction," *Science*, **334**, 333–337 (2011).
[2] J. Zhao, B. Li, Z. N. Chen, and C.-W. Qiu, "Redirection of sound waves using acoustic metasurface," *Applied Physics Letters*, **103**, 151604 (2013).
[3] Y. Xie, W. Wang, H. Chen, A. Konneker, B.-I. Popa, and S. A. Cummer, "Wavefront modulation and subwave length diffractive acoustics with an acoustic metasurface," *Nature Communications*, **5**, 5553 (2014).
[4] Y. Li, X. Jiang, B. Liang, J.-C. Cheng, and L. Zhang, "Metascreen-based acoustic passive phased array," *Physical Review Applied*, **4**, 024003 (2015).
[5] J. Mei, G. Ma, M. Yang, Z. Yang, W. Wen, and P. Sheng, "Dark acoustic metamaterials as super absorbers for low frequency sound," *Nature Communications*, **3**, 756 (2012).
[6] G. Ma and P. Sheng, "Acoustic metamaterials: From local resonances to broad horizons," *Science Advances*, **2**, e1501595 (2016).
[7] W. Wang, Y. Xie, B.-I. Popa, and S. A. Cummer, "Subwavelength diffractive acoustics and wavefront manipulation with a reflective acoustic metasurface," *Journal of Applied Physics*, **120**, 195103 (2016).
[8] N. M. Estakhri and A. Alù, "Wave-front transformation with gradient metasurfaces," *Physical Review X*, **6**, 041008 (2016).
[9] A. Díaz-Rubio and S. A. Tretyakov, "Acoustic metasurfaces for scattering control: Theory and applications," *Physial Review B*, **96**, 125409 (2017).
[10] Y. Ra'di, D. L. Sounas, and A. Alù, "Metagratings: Beyond the limits of graded metasurfaces for wavefront conrol," *Physical Review Letters*, **119**, 067404 (2017).
[11] K. Sun, Y. Fan, S. Chen, Y. Yang, J. Li, Q. Fu, and F. Zhang, "Highly efficient transmissive wavefront steering with acoustic metagratings composed of Helmholtz resonators," *Materials & Design*, **224**, 111352 (2022).
[12] P. M. Morse and K. U. Ingard, *Theoretical Acoustics*, Princeton University Press, Princeton, NJ (1968).
[13] F. Fahy and P. Gardonio, *Sound and Structural Vibration*, 2nd ed., Academic Press, Oxford (2007).
[14] A. D. Pierce, *Acoustics: An Introduction to Its Physical Principles and Applications*, Acoustical Society of America, Melville, NY (2019).